The Anomaly in the Candidate Microlensing Event PA-99-N2

J.H. An, N.W. Evans, E. Kerins, P. Baillon, S. Calchi-Novati, B.J. Carr, M. Creze, Y. Giraud-Heraud, A. Gould, P. Hewett, et al.

The Anomaly in the Candidate Microlensing Event PA-99-N2

Jin H. An,[1] N. W. Evans,[1] E. Kerins,[2] P. Baillon,[3] S. Calchi Novati,[4] B. J. Carr,[5]
M. Crézé,[6,7] Y. Giraud-Héraud,[6] A. Gould,[8] P. Hewett,[1] Ph. Jetzer,[4] J. Kaplan,[6]
S. Paulin-Henriksson,[6] S. J. Smartt,[1] Y. Tsapras,[5] and D. Valls-Gabaud[9]

(The POINT-AGAPE Collaboration)

ABSTRACT

The lightcurve of PA-99-N2, one of the recently announced microlensing candidates towards M31, shows small deviations from the standard Paczyński form. We explore a number of possible explanations, including correlations with the seeing, the parallax effect and a binary lens. We find that the observations are consistent with an unresolved RGB or AGB star in M31 being microlensed by a binary lens. We find that the best fit binary lens mass ratio is $\sim 1.2 \times 10^{-2}$, which is one of most extreme values found for a binary lens so far. If both the source and lens lie in the M31 disk, then the standard M31 model predicts the probable mass range of the system to be 0.02-3.6 $\mathcal{M}_\odot$ (95% confidence limit). In this scenario, the mass of the secondary component is therefore likely to be below the hydrogen-burning limit. On the other hand, if a compact halo object in M31 is lensing a disk or spheroid source, then the total lens mass is likely to lie between 0.09-32 $\mathcal{M}_\odot$, which is consistent with the primary being a stellar remnant and the secondary a low mass star or brown dwarf. The optical depth (or alternatively the differential rate) along the line of sight toward the event indicates that a halo lens is more likely than a stellar lens provided that dark compact objects comprise no less than 15% (or 5%) of haloes.

Subject headings: gravitational lensing — galaxies: individual (M31) — cosmology: dark matter

1. Introduction

The POINT-AGAPE[10] collaboration is a part of a wider group of investigators monitoring M31 (e.g., Ansari et al. 1997; Calchi Novati et al. 2002, 2003) for the purpose of discovering microlensing events, and, in particular, gradients in the rate of events that should be induced by the high inclination of the M31 disk (Crotts 1992; Baillon et al. 1993), so as to infer the presence of dark compact objects in the M31 halo. Recently, the POINT-AGAPE

[1]Institute of Astronomy, University of Cambridge, Madingley Road, Cambridge CB3 0HA, UK

[2]Astrophysics Research Institute, Liverpool John Moores University, 12 Quays House, Egerton Wharf, Birkenhead CH41 1LD, UK

[3]CERN, CH-1211 Genève 23, Switzerland

[4]Institut für Theoretische Physik, Universität Zürich, Winterthurerstrasse 190, CH-8057 Zürich, Switzerland

[5]Astronomy Unit, School of Mathematical Sciences, Queen Mary, University of London, Mile End Road, London E1 4NS, UK

[6]Laboratoire de Physique Corpusculaire et Cosmologie, Collège de France, 11 Place Marcelin Berthelot, F-75231 Paris, France

[7]Université Bretagne-Sud, Campus de Tohannic, BP 573, F-56017 Vannes Cedex, France

[8]Department of Astronomy, Ohio State University, 140 West 18th Avenue, Columbus, OH 43210, USA

[9]Laboratoire d'Astrophysique, Observatoire Midi-Pyrénées, 14 Avenue Edouard Belin, F-31400 Toulouse, France

[10]Pixel-lensing Observations on the Isaac Newton Telescope - Andromeda Galaxy Amplified Pixels Experiment

collaboration announced the discovery of four high signal-to-noise ratio candidate events in the data taken during 1999 and 2000 seasons(Paulin-Henriksson et al. 2003, see also Aurière et al. 2001 and Paulin-Henriksson et al. 2002). The MEGA[11] collaboration has also reported provisional events (de Jong et al. 2003).

This paper studies one of the candidate events, PA-99-N2, which was reported to exhibit an anomaly in its lightcurve. Provided that this is not due to any small but systematic photometric error, some physical mechanism behind this behavior must be sought. This is a productive avenue to explore as it is possible to infer some properties of the lens or source from the deviations from the standard Paczyński form. Here, we show that the observed deviations are consistent with being due to the close approach to a caustic in a binary lens. We calculate the parameters of the best fit binary solutions and discuss their implications.

2. The Anomaly

2.1. The Data

The POINT-AGAPE collaboration has acquired M31 imaging data for three seasons using the Wide Field Camera on the 2.5 m Isaac Newton Telescope located at La Palma, the Canary Islands, Spain. The full analysis of this data set is in progress. Paulin-Henriksson et al. (2003) reported four microlensing candidate events in the first two seasons of data with full-width half-maximum timescales less than 25 days and with flux variations greater than that of a 21st magnitude star (in R band). Among them is PA-99-N2, which is the second event identified in the northern field with a maximum during the 1999 season. It is a very bright event (at maximum) with high signal-to-noise ratio, lying at $22'03''$ ($\sim$5 kpc in projected distance) from the center of M31. Other characteristics are listed in Table 1 of Paulin-Henriksson et al. (2003). The event was observed in three bands, close to the Sloan g', r' and i' filters. As are all POINT-AGAPE observations, the data have been reduced and analyzed using the superpixel method (Calchi Novati et al. 2002; Paulin-Henriksson et al. 2003). The transformation to (Johnson/Cousins) VRI is derived from the observations of Haiman et al. (1994).

Figure 1 shows the lightcurve of PA-99-N2 resulting from the analysis based on the superpixel method in all three bands for the 1999 season. In Figure 2, we also present the residuals from the best fit standard Paczyński lightcurve (PL). There are 65 datapoints in g', 102 in r' and 45 in i'. The lightcurve is flat during the 2000 and 2001 seasons. Visual inspection of the lightcurve shows that there are systematic deviations around JD$'$ 65, which have the same pattern in the g' and r' bands at the same times (there were no i' observations made at the time of anomaly). Henceforth, JD$'$ denotes the Julian Date minus 2451392.5. In Figure 3, we plot the daily averaged g' datapoints against the daily averaged r' datapoints whenever those two band observations are available for the same night. The excellent linear correlation between them confirms the achromaticity of the variable fluxes including the anomalies in the lightcurve. The standard Paczyński fit to daily averaged datapoints gives a χ^2 per degree of freedom of 3.1 (Paulin-Henriksson et al. 2003), which indicates that the deviations are statistically significant.

The photometric recalibration (Calchi Novati et al. 2002; Paulin-Henriksson et al. 2003) of the superpixel method may lead to some concern that the deviations are an artifact of the reduction pipeline. We find a statistical correlation between the seeing and residuals of the superpixel flux with respect to the best fit Paczyński curve for the datapoints taken during the deviation (Fig. 4). This raises the concern that the anomaly may be just an artifact due to seeing variations, and that the superpixel method does not make the proper recalibration.

---

[11] Microlensing Exploration of the Galaxy and Andromeda

Although we emphasize that there exists no such correlation for all other datapoints (Fig. 4), it is still worrisome as the superpixel method was not devised for the photometry of bright resolved sources, for which the apparent correlations take place.

To examine the hypothesis that the deviations can be ascribed solely to seeing variations, we model the reported superpixel flux f, when the source is resolved, by

$$f = f_{\text{true}}[1 + \eta(\theta - \theta_0)] \tag{1}$$

where f_{true} is the true flux, θ is the seeing, and η and θ_0 are fit parameters, while $f = f_{\text{true}}$ (i.e., $\eta = 0$) for all the other datapoints. Note that this provides a simple way of describing the correlation of flux with seeing found in Figure 4. When we fit for η and θ_0 by requiring the behavior of the true flux to be described by a Paczyński curve, this results in significant detections of nonzero η's ($\eta_{g'} = -0.020 \pm 0.003$, $\eta_{r'} = -0.043 \pm 0.003$, $\eta_{i'} = -0.06 \pm 0.01$) with an overall better fit to the Paczński curve, as the χ^2 decreases from 824.7 (700.9) to 438.1 (321.1). Here, the first number is from the data for 1999-2000 seasons (488 datapoints), while the second number is from the 1999 season data only (212 datapoints). Figure 5 shows the residuals for this fit. While there is no visible anomaly any more around JD$'$ 65, close inspection reveals that the lightcurve is still not entirely consistent with Paczyński curve; the datapoints lie systematically below the rising parts of the model lightcurve (in particular, $55 < \text{JD}' < 67$) and the datapoints lie above the model in the falling side wing.[12] In other words, although there is a correlation between flux residuals and seeing, this by itself is not enough to explain the shape of the lightcurve.

One way of testing whether the correlation found in Figure 4 is purely statistical or betrays a causal relation is to derive a second lightcurve which makes different assumptions as to the effects of seeing variation on the photometry. We perform fixed-aperture relative photometry of PA-99-N2 on the raw r' frames with respect to stable stars nearby. This is possible for 31 frames near the peak of the event. In fixed-aperture photometry, the same fraction of flux from the source star enters the aperture irrespective of the brightness of the star, for given seeing. The ratio of flux within the aperture between two stars is therefore the same as the intrinsic ratio, regardless of seeing. The linear regression shown in Figure 6 shows consistency between the superpixel and fixed aperture lightcurves, with no outlier worse than 2σ. The residuals versus seeing shown in the inset suggest there is no correlation when seeing is better than $1''\!\!.8$ although the superpixel flux is lower compared to the fixed aperture photometry when seeing is worse than $1''\!\!.8$, which corresponds to the worst outliers at JD$'$ 63 and JD$'$ 69. At outset, we might expect the outliers to have little influence on any fitting result, as the errorbars are large. This is confirmed by adjusting the datapoints with seeing worse than $1''\!\!.8$ to correspond to the fixed-aperture photometry and checking that any results do not change qualitatively. In particular, the measured parameters change by less than the quoted uncertainty. In Figure 7, we present the residuals from a standard Paczyński fit of the fixed-aperture lightcurve. Again, the discrepancy from the Paczyński fit is $\sim$10%, which is larger than the formal error.

The MEGA collaboration (de Jong et al. 2003) have recently published a lightcurve for the same event, derived from a difference image analysis. They plot only the daily-averages for epochs of good seeing. We find that their lightcurve is consistent with the superpixel lightcurve [13]

The seeming consistency of the three methods makes it unlikely that the deviations are caused by the data reduction. Although it is still possible that some unknown systematic problem with the data taking itself could cause such a spurious effect, we have no reason to suspect this at the moment.

---

[12] The pattern of the deviations is reminiscent of the parallax effect and this possibility is explored in Appendix B.

[13] This was judged from a comparison between our superpixel data and their data as read from the lightcurve presented in de Jong et al. (2003).

2.2.   Possible Causes

There are a number of possible origins for the bump in the lightcurve, including (i) intrinsic variability due to either the source star or another neighbouring star, (ii) a close approach to a lensing caustic (Albrow et al. 2002), or (iii) perturbations caused by a binary source (Griest & Hu 1992; Han & Gould 1997, see also Dominik 1998). Parallax effects can also cause perturbations (see also Smith et al. 2002; Gould 1992; Gould, Miralda-Escudé & Bahcall 1994, Appendix B), but the timescale of deviations is typically $\gtrsim 0.25$ yr, much longer than that of the bump in PA-99-N2. Hence, we discount this possibility.

Plots of the rms variation on each pixel of r' band images taken during 2000 and 2001 seasons show no evidence of any additional variable source within the 7×7 superpixel. There is also no evidence for any variation in the light centroid during the course of the event, which might be expected if the lightcurve is being polluted by a nearby variable. This provides good evidence that the bump is not caused by a nearby variable. It is possible that the source itself is variable, but this is not particularly favored because the deviations are achromatic and because the lightcurve during 2000 and 2001 seasons appears to be flat to good accuracy.

A binary source is somewhat disfavored on the grounds that the perturbations to the lightcurve are usually almost periodic. However, this possibility cannot be definitely ruled out.

In the following, we assume that the deviations are caused by a binary lens. We find that there are physically reasonable binary lens models that are consistent with the available photometric data of PA-99-N2 to a high statistical significance.

3.   Binary Lens Model

The most straightforward way of generating fold caustics is with binary lenses. The simplest cases of binary lens lightcurves – a point source in uniform rectilinear motion lensed by a static binary lens – are characterized by six parameters: the ratio of the two masses q, the projected separation in terms of the Einstein ring radius d, the angle at which the source motion crosses the binary axis α, the time t_0 and the distance $u_0 = u(t_0)$ of the closest approach to a fixed reference point[14] and the Einstein timescale t_E. The best fit binary lens lightcurve of PA-99-N2 can be found by searching for the χ^2 minimum in this six-dimensional parameter space using any standard minimization technique. Note that, while two further parameters for each passband are required to relate the lensing magnifications to the observed fluxes, these parameters enter linearly into the fit, and thus, this part of the problem can be decoupled from the rest of the problem and solved directly by separate matrix inversion.

We have carried out this minimization with the first two seasons of data. There are 212 datapoints (65 in g', 102 in r' and 45 in i') from the 1999 season and 276 datapoints (146 in r' and 130 in i') from the 2000 season.[15] We have found a number of possible binary lens models, and their parameters are listed in Table 1. For the formally best fit model (C1), the lightcurve residuals are shown in Figure 8. We find that there exist several binary lens models that lie at a local χ^2 minimum for which the χ^2 difference with respect to the global minimum is quite small. In particular, the two best fit models, C1 and W1, are essentially indistinguishable in terms of their values of χ^2. Some of these degeneracies would have been broken if the ~20-day observation gap between JD$'$ 72 and JD$'$

---

[14]Following Albrow et al. (2002), the reference point is chosen to be either the center of the mass if $d \leq 1$, or the primary-lens position shifted toward the secondary by the zeroth order correction, $[(1 + q^{-1})d]^{-1}$ if $d \geq 1$.

[15]The difference of the quoted number of datapoints between Paulin-Henriksson et al. (2003) and this paper is because Paulin-Henriksson et al. (2003) used daily averaged datapoints while here we use a single point for each nonfaulty frame.

91 had been regularly covered (for example, Model C2 predicts a cusp grazing near JD$'$ 74 and Model W1$'$ shows a second bump around JD$'$ 77) while others are much more difficult to discriminate.

From Table 1, the timescale of the two best fit binary models are 125.0 ± 7.2 days (C1) and 132.3 ± 7.2 days (W1). In either case, the timescale is larger than $\sim$92 days reported by Paulin-Henriksson et al. (2003) under the assumption of a single point mass lens. This may be expected from the fact that the binary fit possesses a higher maximum amplification. Examination of images taken well after the event shows no resolved star in the vicinity of PA-99-N2. On the other hand, a barely resolved nearby star at this approximate location in our r' band image is measured to have a flux of 7 ADU s^{-1} (Paulin-Henriksson 2002). However, the best estimate of the r' band source flux of PA-99-N2 from the Paczyński fit is 7.90 ± 0.42 ADU s^{-1} and thus nominally inconsistent with it being unresolved at baseline at the 2σ level. This problem is ameliorated with the binary fit, as the source is predicted to be fainter, namely 4.76 ± 0.34 ADU s^{-1} (C1) or 4.55 ± 0.33 ADU s^{-1} (W1), well below the detection limit of a resolved star.

Using the transformation of Paulin-Henriksson (2002), the baseline source flux is calculated as $V = 23.44 \pm 0.09$, which is the average of the results for the two best fit models. The source color is determined from the achromaticity of the lightcurve – the slope of the linear regression line in Figure 3 is directly related to the instrumental $g'_{\mathrm{I}} - r'_{\mathrm{I}}$ color, which, in turn, can be translated into $V - R = 0.983 \pm 0.013$. Similarly, the linear regression involving i' band flux provides the second color $V - I = 2.233 \pm 0.020$. These colors are roughly consistent with that of an early M giant (Bessell & Brett 1988) with $T_{\mathrm{eff}} \simeq 3700$ K and $\log g \simeq 1$ (Lejeune, Cuisinier & Buser 1997), although secure identification is subject to uncertainties due to unknown reddening, metallicity, and mass of the source. In principle, one can estimate the reddening from two color measurements, provided that we know the intrinsic relation between the two colors and the proper reddening law. Here, if we assume that the local M giants sample of Fluks et al. (1994) defines an intrinsic $(V - R)$-$(V - I)$ relation and that the redding law is described by Cardelli, Clayton & Mathis (1989) with $R_V = 3.1$, then we get the extinction, $A_V = 0.54 \pm 0.21$ and the dereddened colors of the source, $(V - R)_0 = 0.85 \pm 0.05$ and $(V - I)_0 = 1.95 \pm 0.11$. While the estimated extinction appears to be rather large, it is not unreasonable considering that the Galactic foreground extinction towards M31 is estimated to be $A_V = 0.2 \sim 0.25$ (Burstein & Heiles 1982; Schlegel, Finkbeiner & Davis 1998). With the distance modulus of M31 $(m - M)_{\mathrm{M31}} = 24.47$ (Holland 1998; Stanek & Garnavich 1998), the absolute magnitude of the source is then $M_V \sim -1.6$, which, combined with its intrinsic color, locates the source on the color-magnitude diagram as a member of the asymptotic giant branch or the red giant branch of metal-rich populations. This suggests that the source probably lies in the M31 disk rather than the metal-poor spheroid.

The color and the magnitude of the source can be combined to provide an estimate of the angular source radius θ_*. This can be done using an empirical calibration of the color with the surface brightness, such as that of van Belle (1999). For the source star of PA-99-N2, the calibration of van Belle (1999), combined with the $(V - I)$-$(V - K)$ correlations of Bessell & Brett (1988), provides the measurement of its angular radius $\theta_* = 0.51 \pm 0.06$ μas. We note that the result is insensitive to the extinction estimate unless the reddening law through the line of sight is abnormal. That is,

$$\frac{(\delta\theta_*)_{\delta A_V}}{\theta_*} = \frac{\ln 10}{5}\left[1 - 1.115\,\frac{d(V - K)}{d(V - I)}\frac{E(V - I)}{A_V}\right]\delta A_V, \qquad (2)$$

and so, with $d(V - K)/d(V - I) \simeq 1.67$ (Bessell & Brett 1988) and $R_{VI} = 1.92$ (Cardelli et al. 1989), even if A_V were mismeasured by $\sim$0.4 mag, the resultant error in θ_* would be only $\sim$0.5%.[16] We also check the result with a different calibration based on $V - I$ (Beuermann, Baraffe & Hauschildt 1999), and get a consistent answer

---

[16]The effect of extinction is somewhat larger if the reddening law follows $R_{VI} = 2.41$ (Schlegel et al. 1998), that is, $\delta \ln \theta_* / \delta A_V \simeq 0.1$.

$\theta_* = 0.51 \pm 0.05$ μas. The corresponding linear radius of the source is $\sim$85 R$_\odot$, and the implied surface gravity

$$\log\left(\frac{g}{\mathrm{cm\ s^{-2}}}\right) = 0.566 + \log\left(\frac{\mathcal{M}}{\mathcal{M}_\odot}\right) - 2\log\left(\frac{\theta_*}{0.51\ \mu\mathrm{as}}\right) - 0.4\left[(m-M)_{\mathrm{M31}} - 24.47\right], \tag{3}$$

is also consistent with the source being a giant. There is some evidence for the presence of finite source size effects in the lightcurve and this, combined with the above estimate of the angular source size, allows us to infer further properties of the source. This is explored in Appendix A.

4.   The Nature of the Lens

The optical depths of different lens populations may be used to assess the likely nature of the lens. The advantage of using the optical depths for this purpose is that they are reasonably robust. Analysis of the timescale or other parameters when available can give further clues as to the nature of the lens, although this is usually more model-dependent. Here, we provide the assessment of the most probable lens population using the optical depth, the observed event duration and the constraints on the lens-source relative proper motion. Each level of assessment exploits more of the available information but requires more model assumptions.

Optical depth evaluations require an assumed spatial distribution for the lenses and sources. We consider the M31 disk and spheroid to be plausible locations for the source and for a stellar lens. We consider massive compact halo objects (MACHOs) in the M31 and the Milky Way dark haloes to be additional possibilities for the lens. The M31 disk is taken to have a double-exponential density profile with a scale length of 5.8 kpc, scale height of 0.4 kpc and central density of 0.4 $\mathcal{M}_\odot$ pc^{-3} (e.g., Hodge 1992; Kerins et al. 2001). For the spheroid, we adopt the flattened power-law distribution of Reitzel, Guhathakurta & Gould (1998) with a core radius of 1 kpc and central density of 5 $\mathcal{M}_\odot$ pc^{-3}. The M31 and Milky Way haloes are taken to be near-isothermal spheres as in Kerins et al. (2001), with both haloes truncated at 100 kpc. We assume that the MACHOs comprise 20% of the total halo mass (Alcock et al. 2000). The combined mass distribution of the M31 populations provide a good fit to the rotation curve (Kent 1989) and to the radially-averaged R-band surface brightness profile (Walterbos & Kennicutt 1987) for reasonable stellar mass-to-light ratios.

Table 2 lists the optical depth τ for the various combinations of lens and source populations. To compute the relative likelihood of the lens and source combinations, the relative density of the spheroid and disk source populations must be taken into account. At the location of PA-99-N2, the disk surface luminosity density is 4.8 times larger than that of the spheroid for our assumed model. (Strictly speaking, the proper ratio of the source density should be that of the specific surface density constrained by the observed source color and magnitude. Due to the lack of a proper local population model of the disk and spheroid stars at the position of PA-99-N2, we ignore the source magnitude and color measurement.) After factoring in the relative source densities, we find the most likely scenario for PA-99-N2 is a source star in the M31 disk and a lens in the M31 halo, (with probability $P = 0.35$) followed by the disk self lensing ($P = 0.2$) and lensing of a disk star by a spheroid star ($P = 0.18$). A MACHO is the more likely alternative for the lens than a star, provided that MACHOs comprise no less than 15% of the total halo mass. However, if we accept that the metal-rich nature of the source implies a denizen of the M31 disk, then the scenario of a lens in the M31 halo becomes slightly more probable ($P = 0.40$).

To utilize the information on the timescale measurement, further assumptions are required as to the lens and source velocity distributions, as well as the lens mass function. We assume random velocities to be characterised by a Maxwellian distribution with a one-dimensional dispersion $\sigma = 40, 100, 166$ and 156 km s^{-1} for the M31 disk, spheroid, halo and Milky Way halo, respectively. In addition, we include rotational velocity components of 235 and 30 km s^{-1} for the M31 disk and spheroid, respectively. M31 stars are assumed to follow the Solar-

neighborhood mass function, specifically a broken power law where $dn/dm \propto m^{-1.4}$ between 0.01 $\mathcal{M}_\odot$ and 0.5 $\mathcal{M}_\odot$ and $dn/dm \propto m^{-2.2}$ above 0.5 $\mathcal{M}_\odot$, with continuity enforced at the knee (Gould, Bahcall & Flynn 1997). For disk stars the upper mass cut-off is 10 $\mathcal{M}_\odot$, while for spheroid lenses we assume a 1-$\mathcal{M}_\odot$ cut-off. The MACHO mass function is assumed to be a Dirac delta function at 0.5 $\mathcal{M}_\odot$ (Alcock et al. 2000).

It should be stressed that, while we are not in the classical microlensing regime, we can use the classical microlensing rate to compare relative likelihoods. This is because the Einstein timescale is uniquely specified from the fit, and so the pixel-lensing detection efficiency is the same unknown constant for all potential lens populations and can therefore cancels out in any comparison. Similarly, the source magnitude is also specified by the fit, and we therefore do not need to make any assumptions regarding the M31 stellar luminosity function.

Table 2 then shows the differential microlensing rate per source, $d\Gamma/dt_{\rm E}$, evaluated at $t_{\rm E,0} = 125.0 \pm 7.2$ days. The most likely scenario for this case is an M31 MACHO lensing a disk star ($P = 0.41$), followed by a disk source lensed by a Milky Way MACHO ($P = 0.27$) and then disk self lensing ($P = 0.11$). While this result is broadly consistent with those derived from the optical depth values, the observed timescale lends greater preference to MACHOs as a probable lens population for our assumed model. Note too that if we use differential rates to make the judgement on the origin of the lens, then a MACHO is more likely than a stellar lens provided MACHOs comprise more than 5% of the M31 and Milky Way haloes.

Figure 9 shows the posterior probability for the lens mass for each combination of lens and source when the timescale information is considered. Here, for the case of MACHO lenses, we relax the assumption of a MACHO being 0.5 $\mathcal{M}_\odot$. But, MACHOs are still assumed to be a population with a unique characteristic mass. If the lens is a MACHO in the Milky Way halo, the corresponding 95% confidence interval on its mass is 0.04-13 $\mathcal{M}_\odot$. Similarly, if a compact object in the M31 halo is responsible for the event, its mass is predicted to lie between 0.09-32 $\mathcal{M}_\odot$ (95% confidence; the disk source) or 0.06-30 $\mathcal{M}_\odot$ (95% confidence; the spheroid source). While both of these mass ranges are quite broad, they tend to favor an interpretation of the MACHO as a stellar remnant or primordial black hole. On the other hand, if PA-99-N2 is a disk self-lensing event, the most probable lens mass is 0.5 $\mathcal{M}_\odot$(which is at the break of the mass function), and the associated 95% confidence interval is 0.02-3.6 $\mathcal{M}_\odot$. In this case, the mass of the primary is consistent with it being a typical low mass disk star, and the mass of the secondary lies below the hydrogen-burning limit at better than the 95% confidence limit. The case of a spheroid source and a disk lens leads to a similar mass estimate (0.02-4.7 $\mathcal{M}_\odot$), while a spheroid lens results in a somewhat narrower mass range (0.02-1 $\mathcal{M}_\odot$) due to the lowering of the upper mass cut-off compared with the disk mass function.

5. Conclusions

We have studied the anomaly in the lightcurve of PA-99-N2. Although there are other possibilities, the assumption of a binary lens provides the most economical explanation of the data. The lens may lie either in the M31 disk/spheroid or the Milky Way/M31 haloes. If the lens lies in the disk/spheroid, the primary is a low mass star. Its companion lies below the hydrogen burning limit with 95% confidence. This would makes it the most distant brown dwarf so far discovered. If the lens lies in the halo, then the primary is most probably a stellar remnant and its companion either a brown dwarf or low mass star.

A.   The Finite Source Effect and the Proper Motion Constraint

When a caustic passes close to a source star, the point-source approximation is sometimes no longer valid. If this "finite source" effect is large enough, the lightcurve can be analyzed to derive an additional parameter $\rho_* = \theta_*/\theta_E$, where θ_E is the angular Einstein ring radius. However, we see that the point-source approximation is already good for the lightcurve of PA-99-N2, and so the finite source effect is not expected to be detected with a high statistical significance. Hence, we do not perform a full search for the best fit finite-source binary-lens model in the seven-dimensional parameter space. Instead, we check whether the deviations of finite-source lightcurves near the best fit binary-lens model are consistent with the observations.

In fact, we find a marginal improvement of the fit by incorporating the finite source effect. A restricted search around the best fit point-source model C1 yields a model (FS in Tab. 1) with a smaller χ^2 than that of C1 by 4.9. We note that, while the geometry of the binary lens – d and q – has been driven to move along the principal conjugate direction (towards the smaller q), the measurements of most other parameters are only minimally affected by the incorporation of the finite source effect. In particular, the timescale and the source flux are changed only by $\lesssim 0.5\%$, which is an order of magnitude smaller than their associated uncertainties. The limiting value when the finite source fit is no better than the point source fit is $\rho_* < 2.06 \times 10^{-2}$ (formally corresponding to $\Delta\chi^2 < 4.9$). Combining this with the measurement of t_E and θ_* (see § 3) provides us with the constraint on the angular Einstein ring size θ_E and the lens-source relative proper motion $\mu_{\rm rel}$;

$$\theta_E \left(= \theta_* \rho_*^{-1}\right) \gtrsim 25 \ \mu\text{as} \tag{A1a}$$

$$\mu_{\rm rel} \left(= \theta_E t_E^{-1}\right) \gtrsim 0.20 \ \mu\text{as day}^{-1} = 3.4 \times 10^2 \ \text{km s}^{-1} \ \text{Mpc}^{-1}. \tag{A1b}$$

Caution should be used in interpreting these limits, as the uncertainties may not properly include systematic effects such as uncertainty in the color transformations or any possible problems in the photometry for the critical three nights data over which finite source effects are detected. For this reason, we distinguish these from other more robust results and have first presented an analysis without any constraint on the proper motion. Nonetheless, we note that, if we combine the limit on the angular Einstein radius with the distance to M31, the implied separation of the two binary lens components (for M31 lenses) is $\gtrsim 10$ AU.

We incorporate the lens-source relative proper motion information into the assessment of the nature of the lens by deriving the differential microlensing rate per source, $d\Gamma/(dt_E d\mu_{\rm rel})$, averaged over the probability distribution of $\mu_{\rm rel}$ inferred from the finite source effect on the observed lightcurve. Here, the differential microlensing rate per source can be found for the case of Maxwellian lens and source random velocity distributions by

$$\frac{d^2\Gamma}{dt_E \, d\mu_{\rm rel}} = \int \int \frac{4\mu_{\rm rel}^3}{\sigma_T^2 \Sigma_S} \exp\left(-\frac{v_S^2}{2\sigma_T^2}\right) \exp\left(-\frac{\mu_{\rm rel}^2 D_L^2}{2\sigma_T^2}\right) I_0\left(\frac{\mu_{\rm rel} D_L v_S}{\sigma_T^2}\right) \frac{D_L^7}{D_S(D_S - D_L)} \rho_S(D_S)\rho_L(D_L)\psi(m)dD_S dm, \tag{A2}$$

where D_S is the distance to the source, ρ_L and ρ_S are the lens and source mass densities, Σ_S is the source surface mass density, $\psi(m) = \rho_L^{-1}(dn/dm)$ is the lens mass function normalized to the lens mass density, and $I_0(y)$ is the Modified Bessel function of order zero. Also note that the distance to the lens, D_L is in fact a function of D_S and the lens mass m for a fixed t_E and $\mu_{\rm rel}$. Equation (A2) has been derived by attributing all random velocities to the lens and all rotational motions to the source. The velocity dispersion σ_T is therefore a combination of the lens velocity dispersion σ_L and source velocity dispersion σ_S projected at the lens location, while v_S is the transverse

component of the difference between source and lens rotation speeds. For Milky Way lenses $\sigma_T \simeq \sigma_L$, while for M31 lenses $\sigma_T \simeq (\sigma_L^2 + \sigma_S^2)^{1/2}$.

In Table 2, we list this averaged differential rate for the same various combinations of the lens and source populations. Note that the absolute normalization of the probability density for μ_{rel} is unknown, and so we have effectively integrated $d^2\Gamma/(dt_E d\mu_{rel})$ over μ_{rel} weighted by its relative probability. Hence, the numerical values of the differential rates are essentially normalized by the peak value of the probability density for μ_{rel}. We find that the derived proper motion constraint overwhelmingly favors an M31 MACHO lens with either a disk or spheroid star being a source. In fact, an M31 halo with a MACHO fraction as small as 1% produces a comparable event rate as that of the stellar lenses.

B.   Seeing Correction Plus Parallax Effects

We have already shown in § 2 that the bump in the lightcurve of PA-99-N2 can be removed by correlated variations with the seeing, but that the resulting lightcurve is still anomalous. Here, we explore the possibility that the remaining anomaly is due to some physical effect. An asymmetry between the rising and falling side of the lightcurve is characteristic of a non-uniform lens motion with respect to the source. The most common cause of this is the Earth's orbital motion around the Sun, referred to as the parallax effect.

We fit the data of PA-99-N2 to equation (1) with f_{true} as the lightcurve of a parallax event. The deviation is consistent with the parallax effect and there are at least four degenerate solutions, listed in Tables 3 and 4. (This arises because it is only an acceleration with respect to the instantaneous relative velocity of the lens that is detected.) However, we regard this as a less likely alternative than the hypothesis of a binary lens, even more so than suggested on purely statistical grounds by the χ^2 difference.

First, using the data in Table 4, the projected velocity of the lens on the observer plane ($\tilde{v}$) is $\sim$20 km s^{-1}. We note that this is an upper limit to the lens-source relative velocity. Already this makes it extremely unlikely that the lens resides in the haloes of either the Milky Way or M31. Only Milky Way disk stars are likely to have such a small relative velocity. The distance to the lens belonging to the Milky Way can be estimated from the parallax, assuming $D_L \ll D_S$, that is,

$$D_L \approx D_L \left(1 - \frac{D_L}{D_S}\right)^{-1} = \frac{c^2 \tilde{r}_E^2}{4G\mathcal{M}} = 0.1227 \text{ kpc } \left(\frac{\mathcal{M}}{\mathcal{M}_\odot}\right)^{-1} \left(\frac{\tilde{r}_E}{\text{AU}}\right)^2. \tag{B1}$$

For a typical lens mass of $\sim$0.5 $\mathcal{M}_\odot$, then the lens distance is $\sim$2 kpc. This corresponds to a vertical height above the Galactic plane of $\sim$700 pc. This is uncomfortably high, as it is twice the scale-height of the thin disk. The location of the lens can be brought within the scaleheight of the thin disk by increasing its mass to $\sim$1 $\mathcal{M}_\odot$, but such an object would surely be directly imaged if it were a normal star. The only possibility that seemingly remains is a disk white dwarf.

In addition to the *a priori* low probability of lensing by a disk white dwarf, the further objection to this scenario – seeing variation plus parallax effect models – is that it is not consistent with the fixed aperture photometry described in § 2. This is evident on inspection of Figure 7, which shows residuals of the fixed aperture photometry together with a number of the models discussed in the text. The best fit binary lens model (C1) clearly describes best the pattern of deviations among various alternatives.

REFERENCES

Albrow, M. D., et al. 2002, ApJ, 572, 1031

Alcock, C., et al. 2000, ApJ, 542, 281

Ansari, R., et al. 1997, A&A, 324, 843

Aurière, M., et al. 2001, ApJ, 553, L137

Baillon, P., Bouquet, A., Giraud-Héraud, Y., & Kaplan, J. 1993, A&A, 277, 1

Bessell, M. S., & Brett, J. M. 1988, PASP, 100, 1134

Beuermann, K., Baraffe, I., & Hauschildt, P. 1999, A&A, 348, 524

Burstein, D., & Heiles, C. 1982, AJ, 87, 1165

Calchi Novati, S., et al. 2002, A&A, 381, 848

Calchi Novati, S., Jetzer, Ph., Scarpetta, G., Giraud-Héraud, Y., Kaplan, J., Paulin-Henriksson, S., & Gould, A. 2003, A&A, 405, 851

Cardelli, J. A., Clayton, G. C., & Mathis, J. S. 1989, ApJ, 345, 245

Crotts, A. P. S. 1992, ApJ, 399, L43

de Jong, J. T. A., et al. 2003, A&A, submitted (astro-ph/0307072)

Dominik, M. 1998, A&A, 329, 361

Fluks, M. A., Plez, B., Thé, P. S., de Winter, D., Westerlund, B. E., & Steenman, H. C. 1994, A&AS, 105, 311

Gould, A. 1992, ApJ, 392, 442

Gould, A., Bahcall, J. N., & Flynn, C. 1997, ApJ, 482, 913

Gould, A., Miralda-Escudé, J., & Bahcall, J. N. 1994, ApJ, 423, L105

Griest, K., & Hu, W. 1992, ApJ, 397, 362

Haiman, Z., et al. 1994, A&A, 286, 725

Hodge, P. 1992, The Andromeda Galaxy (Kluwer: Dordrecht)

Han, C., & Gould, A. 1997, ApJ, 480, 196

Holland, S. 1998, AJ, 115, 1916

Kent, S. M. 1989, AJ, 97, 1614

Kerins, E., et al. 2001, MNRAS, 323, 13

Lejeune, Th., Cuisinier, F., & Buser, R. 1997, A&AS, 125, 229

Paulin-Henriksson, S. 2002, Ph.D. Thesis, Univ. Paris VI.

Paulin-Henriksson, S., et al. 2002, ApJ, 576, L121

Paulin-Henriksson, S., et al. 2003, A&A, 405, 15

Reitzel, D. B., Guhathakurta, P., & Gould, A. 1998, AJ, 116, 707

Schlegel, D. J., Finkbeiner, D. P., & Davis, M. 1998, ApJ, 500, 525

Smith, M. C., et al. 2002, MNRAS, 336, 670

Smith, M. C., Mao, S., & Paczyński, B. 2003, MNRAS, 339, 925

Soszyński, I., et al. 2001, ApJ, 552, 731

Stanek, K. Z., & Garnavich, P. M. 1998, ApJ, 503, L131

van Belle, G. T. 1999, PASP, 111, 1515

Walterbos, R., & Kennicutt, R. 1987, A&AS, 69, 311

Table 1. Binary Lens Models of PA-99-N2

model	$\log d$	$\log q$	t_0 (JD $-$ 2451392.5)	u_0 ($\times 10^{-2}$)	t_E (days)	α [a] (deg)	χ^2	χ^2_{1999} [b]
C1	-0.242 ± 0.020	-1.850 ± 0.096	73.22 ± 0.19	3.60 ± 0.37	125.0 ± 7.2	24.2 ± 2.1	312.5	195.3
W1	0.265 ± 0.021	-1.911 ± 0.111	73.52 ± 0.25	3.40 ± 0.40	132.3 ± 7.2	24.5 ± 2.7	312.7	195.6
W1′	0.126 ± 0.021	-2.57 ± 0.20	75.84 ± 0.10	0.66 ± 0.23	$172. \pm 23.$	4.9 ± 1.0	322.3	205.7
C2	-0.581 ± 0.023	-0.384 ± 0.098	73.18 ± 0.10	2.10 ± 0.49	129.0 ± 7.7	271.5 ± 4.7	345.6	228.8
C3	-0.433 ± 0.049	-0.985 ± 0.156	72.73 ± 0.12	4.09 ± 0.24	121.6 ± 6.6	278.1 ± 3.6	345.7	228.9
W2	0.78 ± 0.10	0.03 ± 0.24	73.17 ± 0.11	1.44 ± 0.32	$195. \pm 28.$	270.7 ± 4.9	346.5	229.8
W3	0.46 ± 0.10	-0.93 ± 0.27	72.72 ± 0.13	3.98 ± 0.23	130.8 ± 6.2	278.5 ± 5.4	349.7	232.9
FS [c]	-0.170 ± 0.047	-2.12 ± 0.20	73.12 ± 0.13	3.86 ± 0.51	124.3 ± 8.5	26.4 ± 2.7	307.6	190.3
PL [d]	$\cdots$	$\cdots$	71.56 ± 0.08	7.47 ± 0.37	91.9 ± 3.7	$\cdots$	824.6	700.8

[a]The fixed reference point of system lies on the right hand side of the moving source path.

[b]The χ^2 only accounting for the 1999 season data.

[c]The best fit finite source model associated with C1. The finite source parameter for this model is derived to be $\rho_* = (1.31 \pm 0.30) \times 10^{-2}$. One may formally interpret that C1 is in fact the best fit model with the constraint that $\rho_* = 0$.

[d]The best fit Paczyński lightcurve. The difference of the errorbars of the parameter measurement and χ^2 compared to Paulin-Henriksson et al. (2003) is because here we use individual datapoints (instead of daily averaged points) and the formal errorbars derived from the local curvature matrix.

Note. — The total number of degrees of freedom is 476 (= 488 datapoints − 12 parameters), except PL where nine parameters are used. The uncertainties for parameters are derived from the local curvature matrix (half the local Hessian of χ^2) except for model W1′, for which they represent the interval of $\chi^2 \leq \chi^2_0 + 1$ where χ^2_0 is the associated local minimum.

Table 2.   Microlensing Optical Depths and Event Rates at the Location of PA-99-N2

lens	source	τ $(\times 10^{-7})$	$d\Gamma/dt_{\rm E}$ $(\times 10^{-9}\ {\rm yr}^{-1}\ {\rm day}^{-1}\ {\rm star}^{-1})$	$\langle d\Gamma/(dt_{\rm E}d\mu_{\rm rel})\rangle$ $(\times 10^{-10}\ P_{\mu_{\rm rel,max}}\ {\rm yr}^{-1}\ {\rm day}^{-1}\ {\rm star}^{-1})$
M31 disk	M31 disk	2.8	0.59	0.25
M31 spheroid		2.5	0.35	0.03
M31 halo		4.8	2.2	4.5
Milky Way halo		2.0	1.5	0
M31 disk	M31 spheroid	1.1	0.22	0.35
M31 spheroid		1.1	0.30	0.02
M31 halo		3.1	1.8	3.6
Milky Way halo		2.0	1.5	0

Note. — For both haloes of M31 and the Milky Way, it is assumed that 0.5 $\mathcal{M}_\odot$ MACHOs comprise 20% of the total mass of dark haloes (Alcock et al. 2000).

Table 3.   Models of PA-99-N2 with a seeing correlation

model	$t_{0,\oplus}$ (JD $-$ 2451392.5)	$u_{0,\oplus}$ $(\times 10^{-2})$	$t_{\rm E,\oplus}$ (days)	χ^2	χ^2_{1999}	Note.
PL0 [a]	71.56 ± 0.08	7.47 ± 0.37	91.9 ± 3.7	824.6	700.8	$\cdots$
PLS [b]	70.39 ± 0.09	3.98 ± 0.40	$148. \pm 12.$	438.1	321.1	$\cdots$
PLA [c]	70.20 ± 0.09	2.98 ± 0.37	$200. \pm 22./192. \pm 20.$	342.5	225.5	$\dot{\mu}_{\rm E} = (4.0 \pm 1.0) \times 10^{-5}\ {\rm day}^{-2}$
XPN	70.32 ± 0.10	4.42 ± 0.63	$134. \pm 17.$	337.4	220.6	$\pi_{\rm E} = (3.0 \pm 1.1) \times 10^{-1}$
XPP	70.38 ± 0.10	4.90 ± 0.60	$121. \pm 13.$	336.5	221.1	$\pi_{\rm E} = (5.1 \pm 0.7) \times 10^{-1}$
XNN	70.29 ± 0.10	-4.07 ± 0.54	$149. \pm 17.$	338.2	221.2	$\pi_{\rm E} = (2.2 \pm 0.7) \times 10^{-1}$
XNP	70.34 ± 0.10	-3.63 ± 0.77	$172. \pm 34.$	337.8	223.2	$\pi_{\rm E} = (3.7 \pm 0.8) \times 10^{-1}$

[a]Same as the model PL in Table 1.

[b]Paczyński curve + seeing correlation from eq. (1).

[c]Point mass lens + uniform acceleration + seeing correlation from eq. (1). Two different values of $t_{\rm E}$ correspond to two degenerate models discovered by Smith, Mao & Paczyński (2003).

Note. — The parameters for models with non-uniform motion are basically for the tangent to the trajectory at the time of the closest approach between the lens and the source ($t = t_0$). The $\dot{\mu}_{\rm E}$ denotes the proper acceleration normalised to the angular Einstein ring size (i.e., $\mu_{\rm E} = \mu_{\rm rel}/\theta_{\rm E}$), while $\pi_{\rm E}$ is the lens-source relative parallax normalised by $\theta_{\rm E}$.

Table 4.   Standard parameterization of parallax models

model	$t_{0,\odot}$ (JD $-$ 2451392.5)	$u_{0,\odot}$ ($\times 10^{-2}$)	$t_{\mathrm{E},\odot}$ (days)	$\tilde{r}_{\mathrm{E}}$ (AU)	ψ (deg)	$\tilde{v}$ (km s^{-1})
XPN	96.2 ± 13.2	-1.6 ± 2.0	$193. \pm 34.$	3.3 ± 1.2	-87.3 ± 4.4	29.9 ± 15.1
XPP	$129.4 \pm\ \ 6.5$	3.5 ± 3.5	$246. \pm 31.$	2.0 ± 0.3	-65.6 ± 8.0	13.9 ± 1.6
XNN	96.7 ± 10.4	-7.2 ± 2.6	$189. \pm 30.$	4.6 ± 1.4	-89.0 ± 7.5	42.3 ± 17.7
XNP	$157.8 \pm\ \ 5.8$	3.2 ± 2.2	$358. \pm 85.$	2.7 ± 0.6	-61.8 ± 4.4	13.1 ± 0.9

Note. — This gives the 5 parameters required to define a parallax lightcurve using the conventional notation found in Soszyński et al. (2001). The projected velocity $\tilde{v} = \mu_{\mathrm{rel}}(D_{\mathrm{L}}^{-1} - D_{\mathrm{S}}^{-1})^{-1} = v_{\mathrm{rel}}[1 - (D_{\mathrm{L}}/D_{\mathrm{S}})]^{-1}$ is found by $\tilde{r}_{\mathrm{E}}/t_{\mathrm{E},\odot}$.
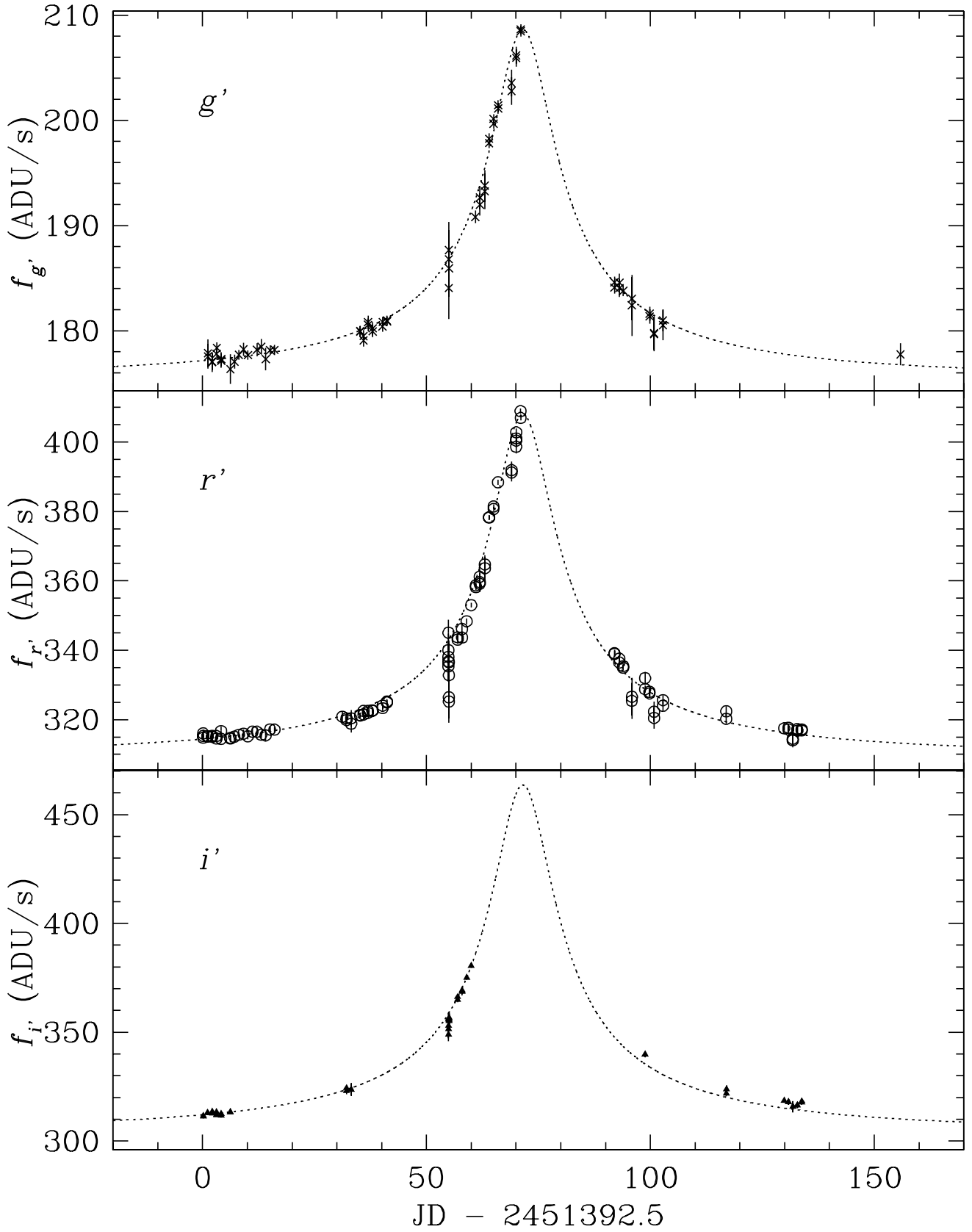
Fig. 1.— Lightcurve of PA-99-N2 in the r', g' and i' bands for the 1999 season. The dotted line shows the best fit Paczyński lightcurve which assumes an isolated point-mass lens. Crosses in the top panel are for g', open circles in the middle panel are for r', and filled triangles in the bottom panel are for i' datapoints.
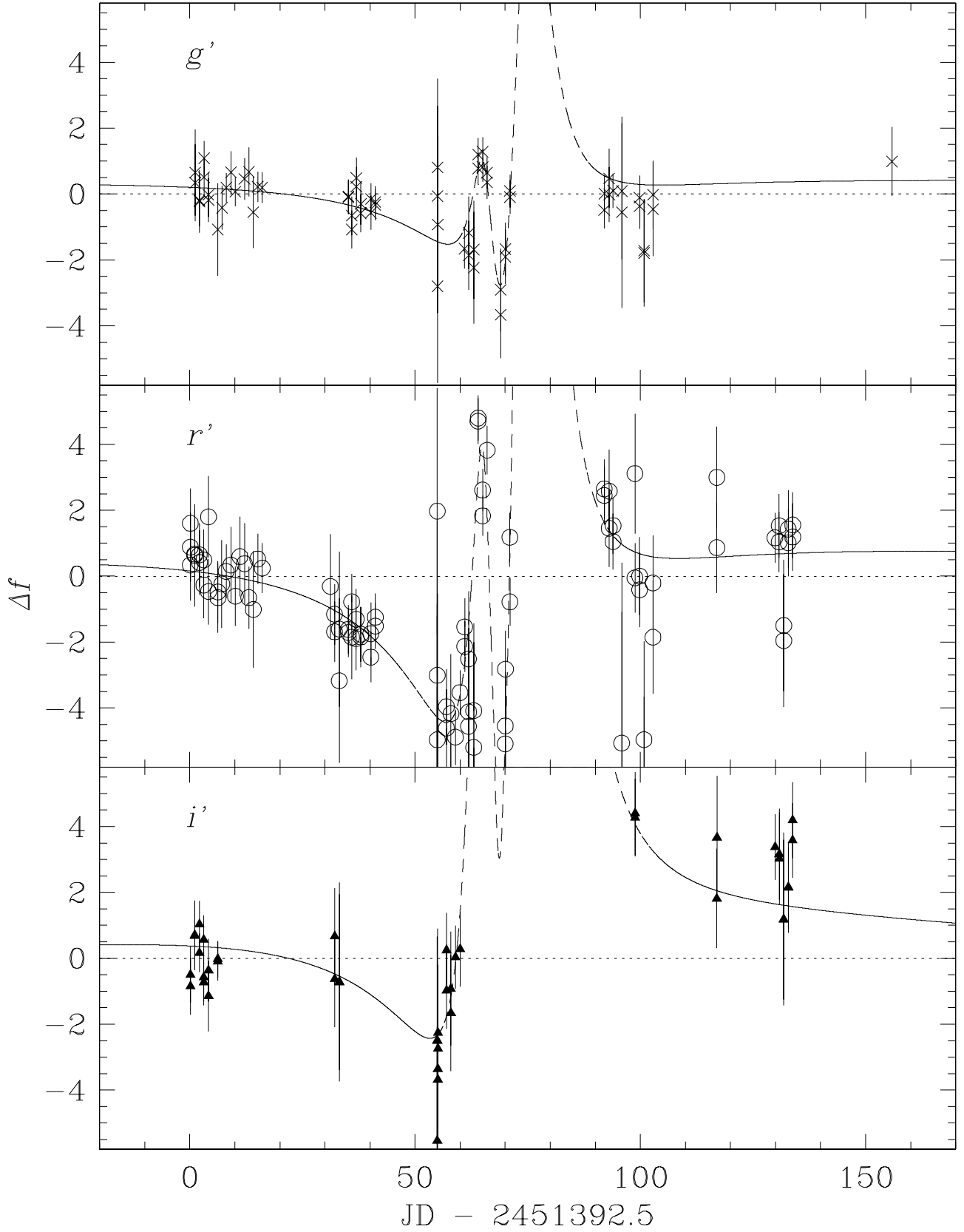
Fig. 2.— Residuals from a standard Paczyński fit. Symbols are the same as Fig. 1. The curve shows the best fit binary lens model (C1).
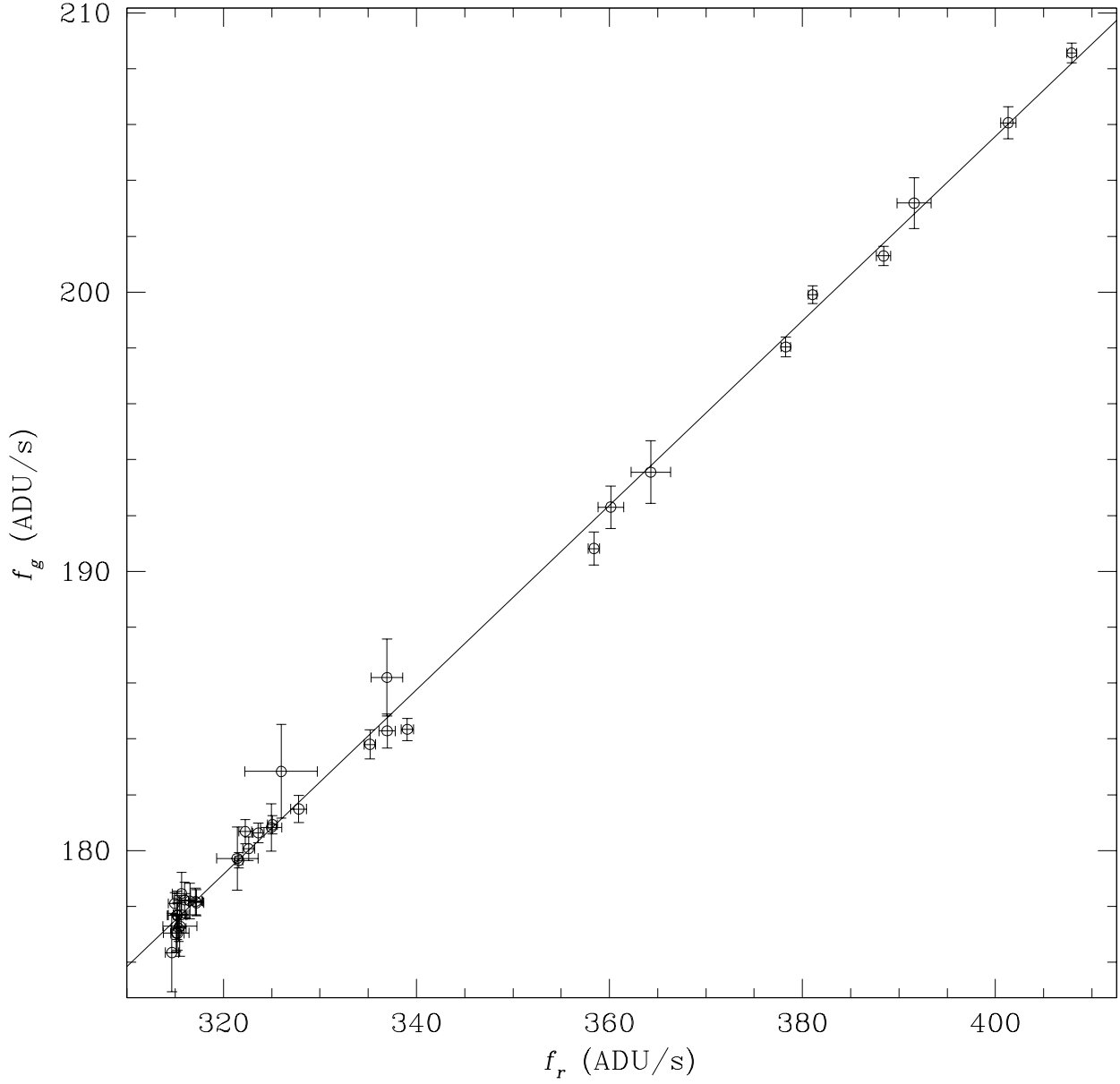
Fig. 3.— Daily averaged g' band flux plotted against r' band flux observed at the same night. Also shown as a solid line is the best fit linear regression line. Note that the slope of this regression line is related to the instrumental color $g'_I - r'_I = -2.5 \log a$.
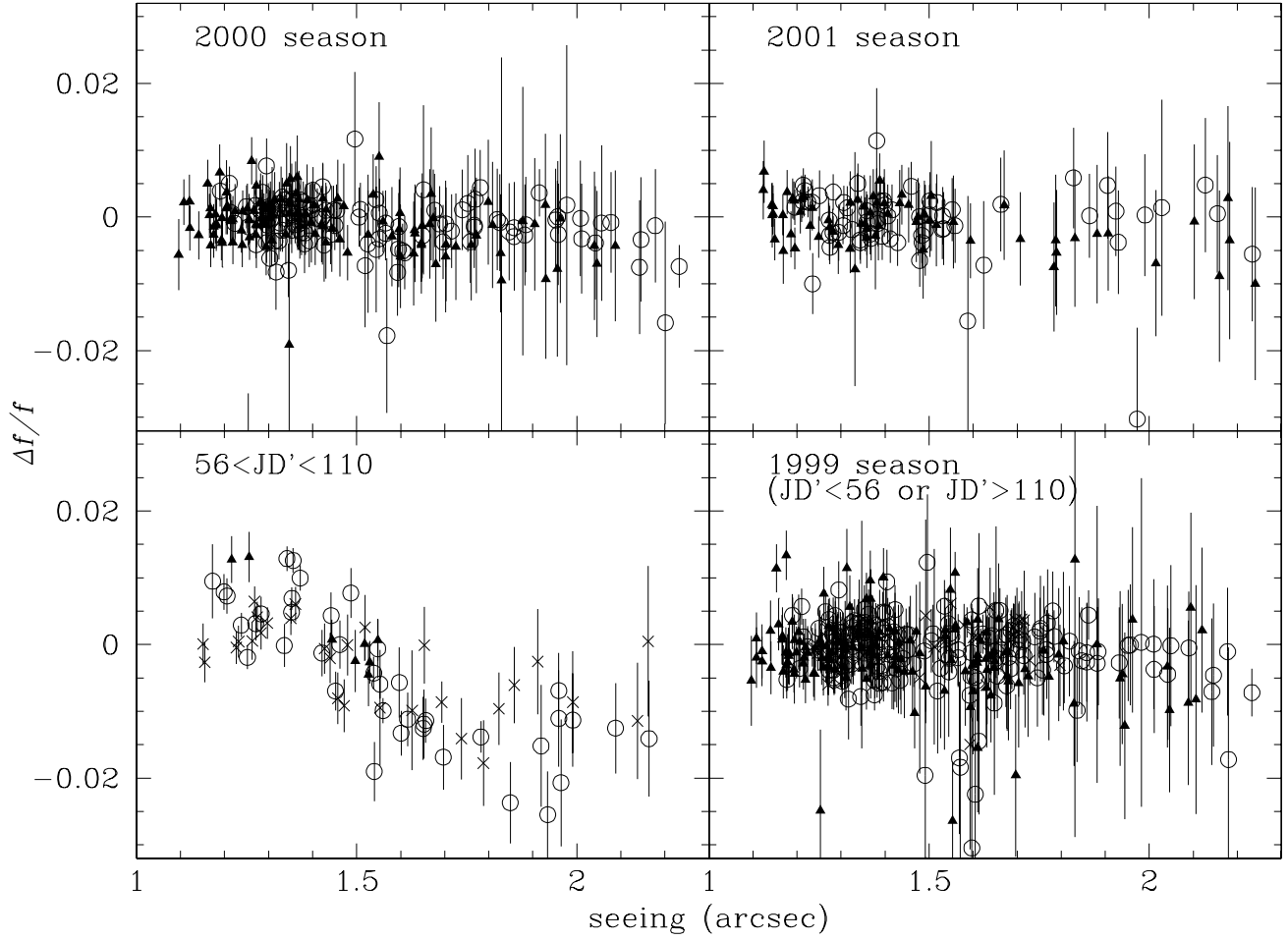
Fig. 4.— Relative residuals versus seeing. Symbols are the same as Fig. 1. For 1999 season, residuals are from the best fit standard Paczyński curve. For 2000 and 2001 seasons, residuals are with respect to flat baseline.
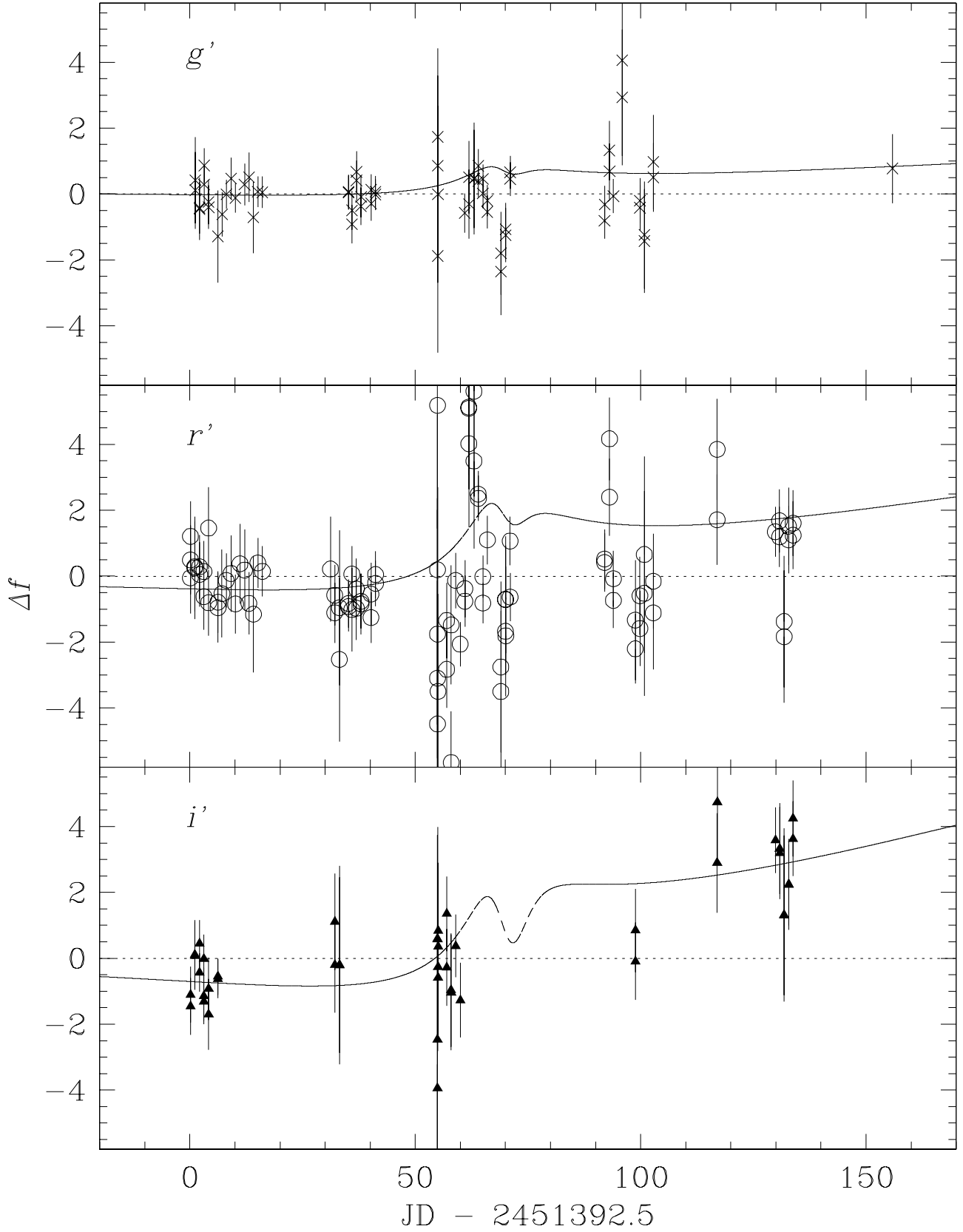
Fig. 5.— Residuals for the Paczyński curve fit with seeing correlation given by eq. (1). Symbols are the same as Fig. 2. The curve shows the pattern of residuals expected for the parallax model (XPN) given in the Appendix B.
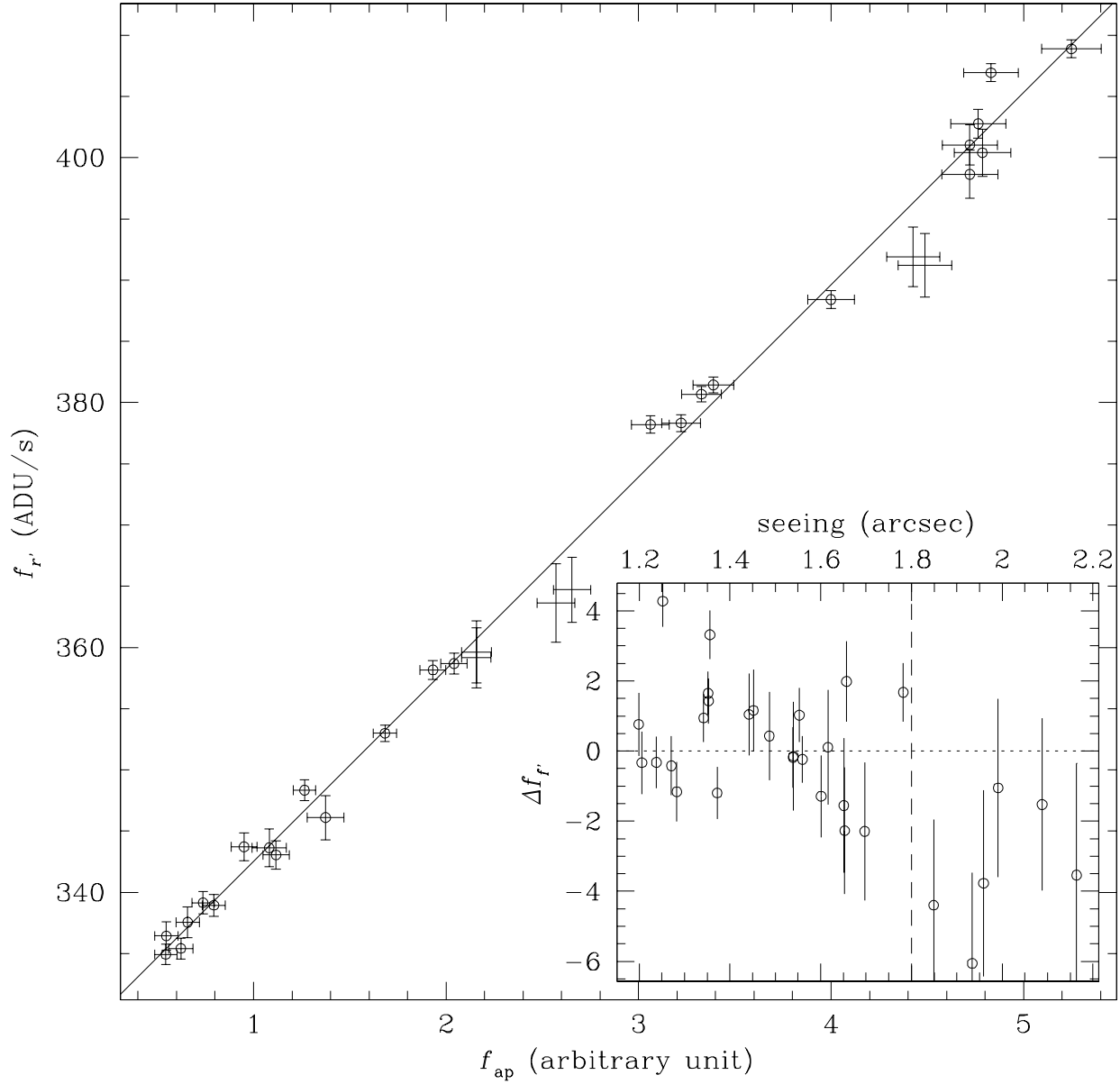
Fig. 6.— Superpixel flux in r' band plotted against the fixed-aperture photometry result. Error bars without points corresponds to the datapoints with seeing worse than $1''\!.8$. The solid line is the best fit linear regression line. Residuals of superpixel flux from this regression versus seeing is also shown in inset.
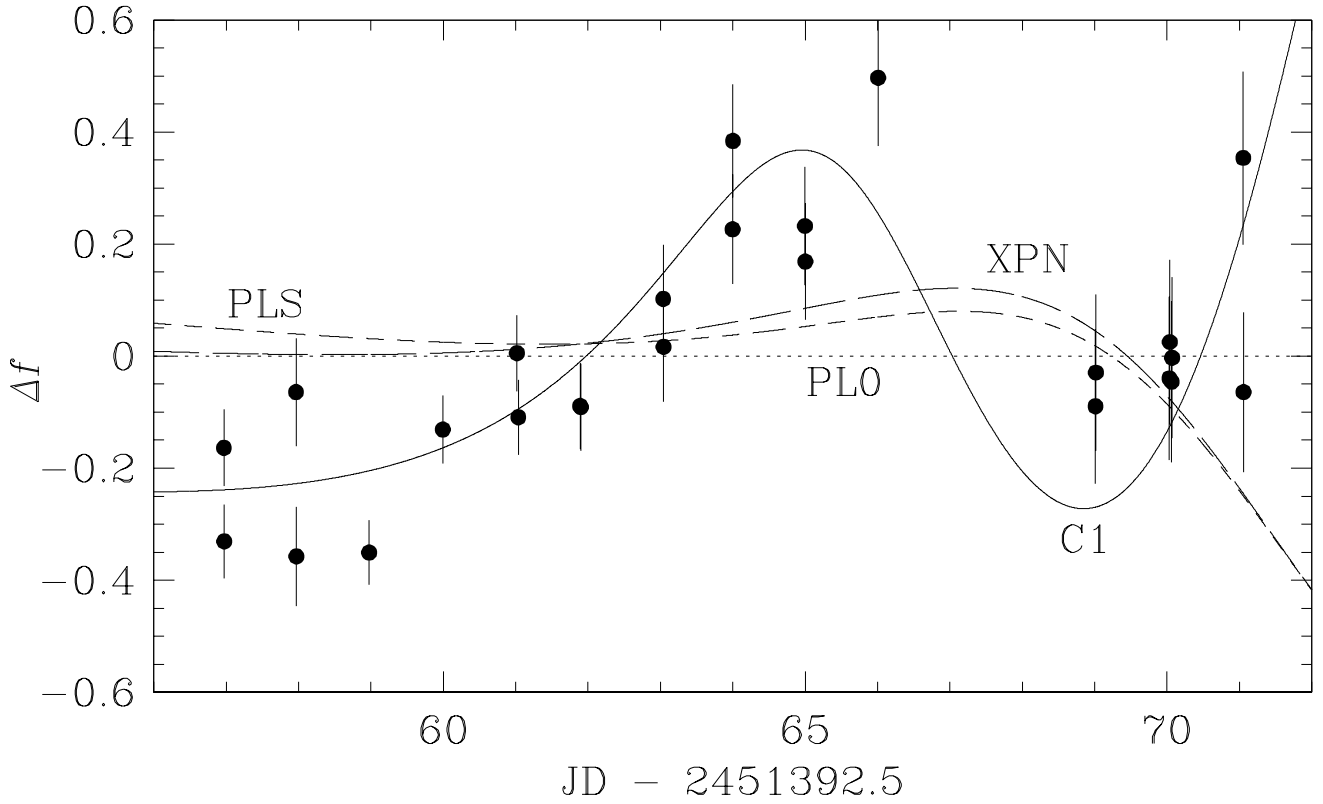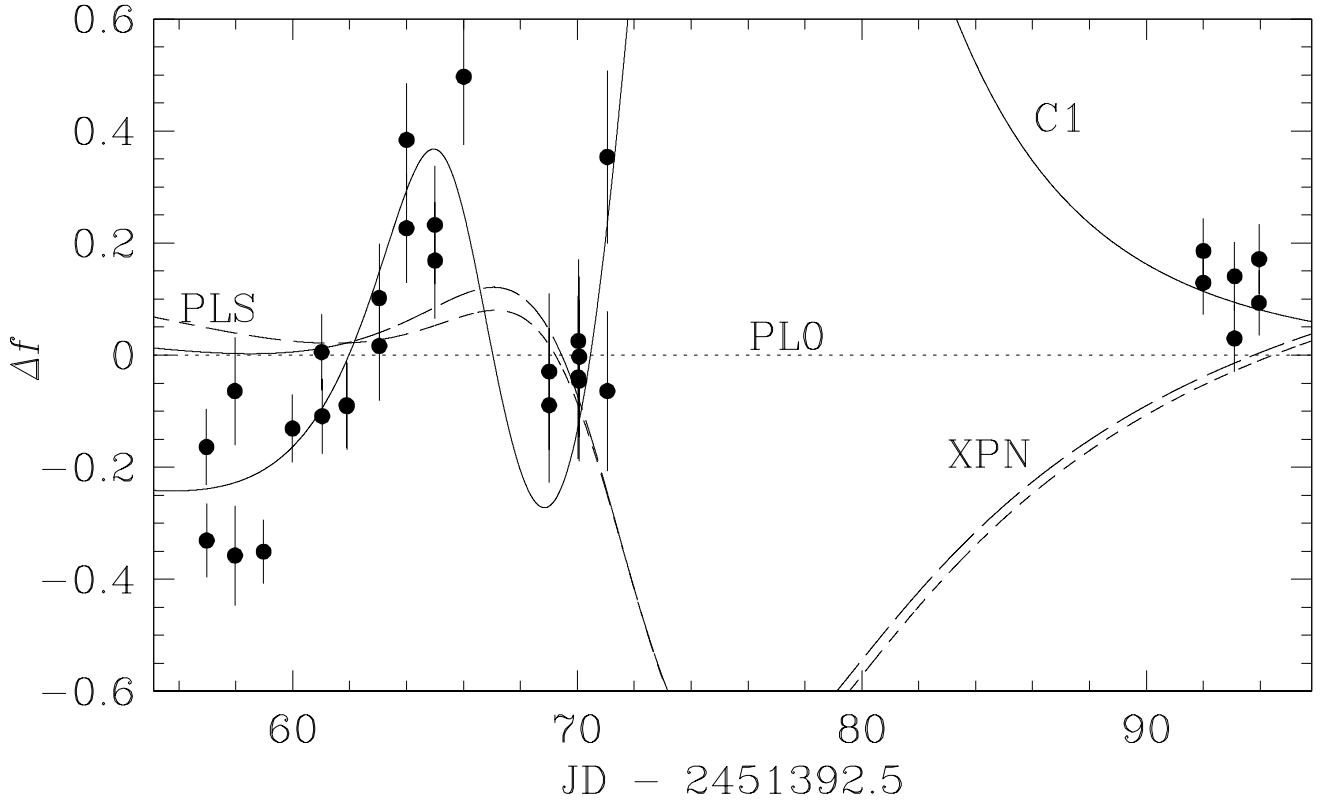
Fig. 7.— Residuals of the fixed-aperture photometry from a standard Paczyński fit. Also shown are a number of models discussed in the text: Paczyński curve with seeing correction (PLS), best fit binary lens model (C1) and best fit parallax model with seeing correction (XPN). For the details, refer to Tables 1 and 3.
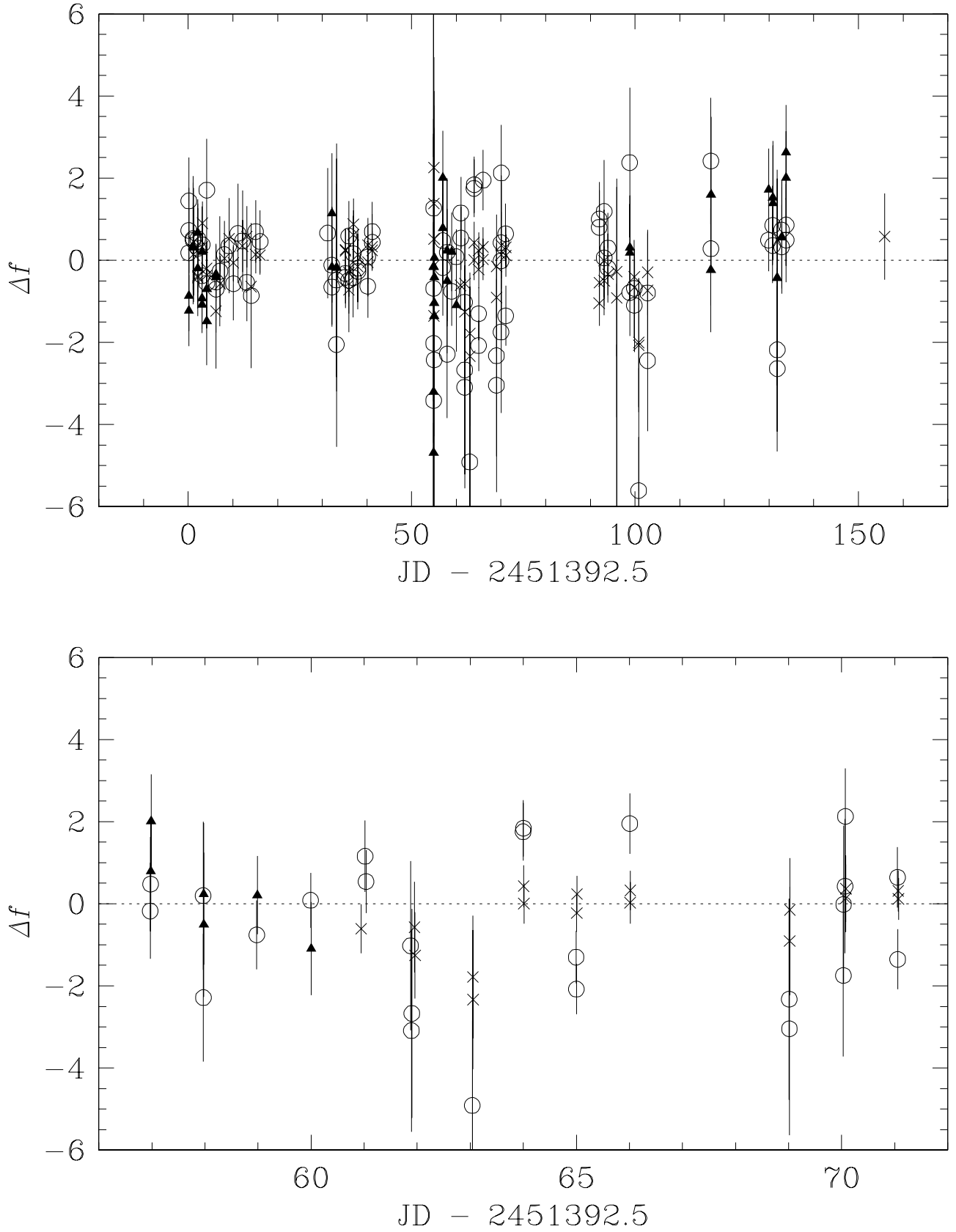
Fig. 8.— Residuals from the best fit binary lens model (C1). Symbols are the same as Fig. 2. The upper panel is for the whole 1999 season while the lower panel zooms in the rising part of the lightcurve near the time of the anomaly.
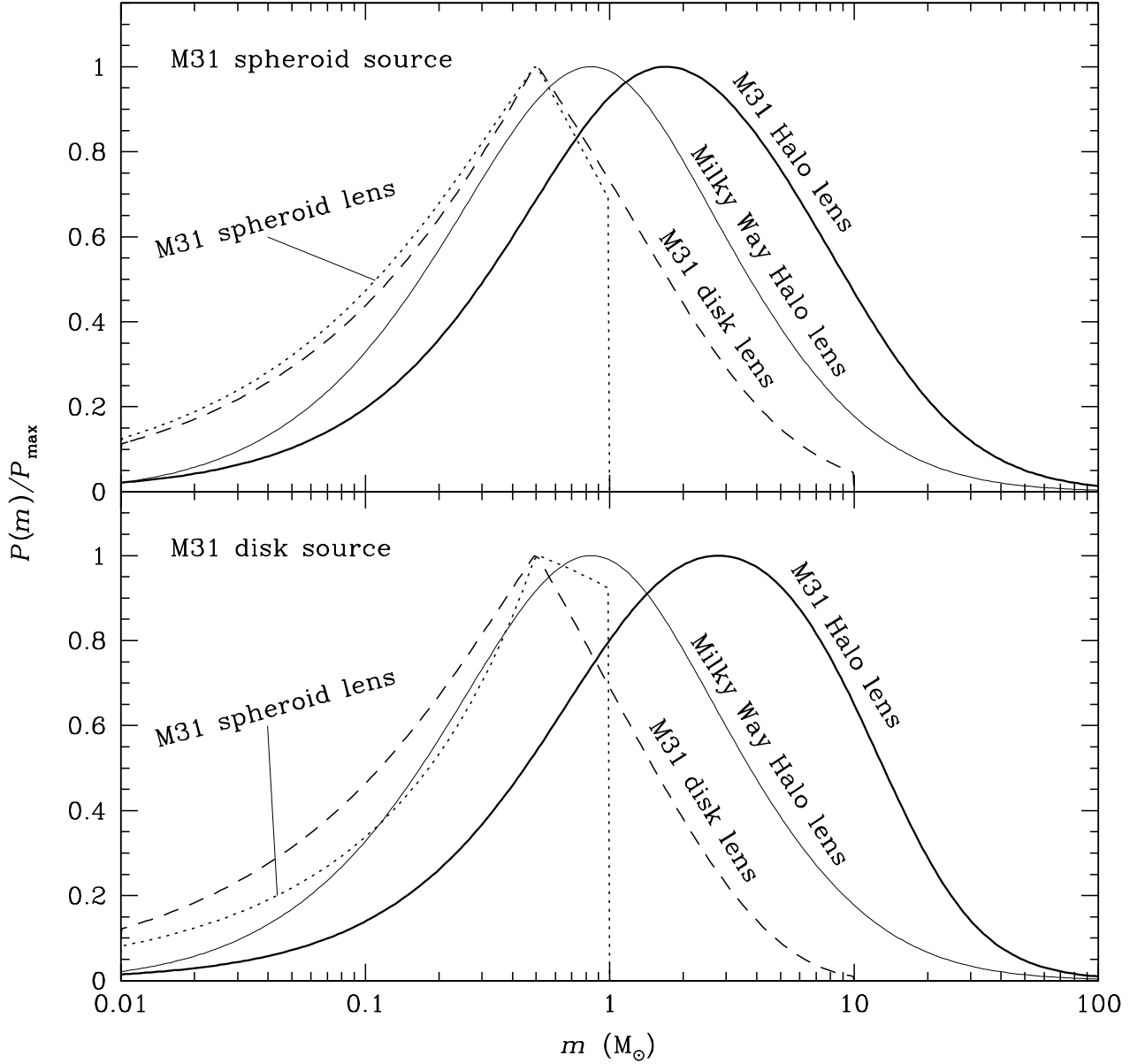
Fig. 9.— Relative probability P (or differential microlensing rate $d^2\Gamma/(dm dt_{\rm E})$) for the lens mass m for different lens locations. The upper (lower) panel assumes that the source lies in the M31 spheroid (or M31 disk). For the halo lenses, these curves show the variation of the differential microlensing rate, $d\Gamma/dt_{\rm E}$ when the halo is comprised of objects of the given mass in entirety. All curves are normalised to the same maximum value $P_{\rm max}$.